Link to publisher's version: *https://doi.org/10.1016/j.ecss.2018.03.027*

Citation: Han Q, Chen D, Guo Y et al (2018) Saltwater-freshwater mixing fluctuation in shallow beach aquifers. Estuarine, Coastal and Shelf Science. 207: 93-103.

Saltwater-freshwater mixing fluctuation in shallow beach aquifers

Qiang Han[1, 2], Daoyi Chen[1, 2], Yakun Guo[2, 3], Wulong Hu[4]

Abstract

Field measurements and numerical simulations demonstrate the existence of an upper saline plume in tidally dominated beaches. The effect of tides on the saltwater-freshwater mixing occurring at both the upper saline plume and lower salt wedge is well understood. However, it is poorly understood whether the tidal driven force acts equally on the mixing behaviours of above two regions and what factors control the mixing fluctuation features. In this study, variable-density, saturated-unsaturated, transient groundwater flow and solute transport numerical models are proposed and performed for saltwater-freshwater mixing subject to tidal forcing on a sloping beach. A range of tidal amplitude, fresh groundwater flux, hydraulic conductivity, beach slope and dispersivity anisotropy are simulated. Based on time sequential salinity data, the gross mixing features are quantified by computing the spatial moments in three different aspects, namely, the centre point, length and width, and the volume (or area in a two-dimensional case). Simulated salinity distribution varies significantly at saltwater-freshwater interfaces. Mixing

[1]School of Environmental Science and Engineering, Tsinghua University, Beijing 100084, P.R. China. Email: hanq12@mails.tsinghua.edu.cn

[2]Ocean Science and Technology Division, Graduate School at Shenzhen, Tsinghua University, Shenzhen 518055, P.R. China. **Corresponding Author Email: chen.daoyi@sz.tsinghua.edu.cn**

[3]School of Engineering, University of Bradford, BD7 1DP, UK. Email: y.guo16@bradford.ac.uk

[4]Hubei Key Laboratory of Theory and Application of Advanced Materials Mechanics, Wuhan University of Technology, Wuhan 430070, P.R. China. E-mail: wulong.hu@whut.edu.cn

characteristics of the upper saline plume greatly differ from those in the salt wedge for both the transient and quasi-steady state. The mixing of the upper saline plume largely inherits the fluctuation characteristics of the sea tide in both the transverse and longitudinal directions when the quasi-steady state is reached. On the other hand, the mixing in the salt wedge is relatively steady and shows little fluctuation. The normalized mixing width and length, mixing volume and the fluctuation amplitude of the mass centre in the upper saline plume are, in general, one-magnitude-order larger than those in the salt wedge region. In the longitudinal direction, tidal amplitude, fresh groundwater flux, hydraulic conductivity and beach slope are significant control factors of fluctuation amplitude. In the transverse direction, tidal amplitude and beach slope are the main control parameters. Very small dispersivity anisotropy (e.g., $\alpha_L/\alpha_T < 5$) could greatly suppress mixing fluctuation in the longitudinal direction. This work underlines the close connection between the sea tides and the upper saline plume in the aspect of mixing, thereby enhancing understanding of the interplay between tidal oscillations and mixing mechanisms in tidally dominated sloping beach systems.

Keywords: *Coastal aquifer; Saltwater-freshwater mixing fluctuation; Tidal effects; Mixing quantification; Upper saline plume; Subterranean estuary*

1 Introduction

Submarine groundwater discharge (SGD) represents an important transport pathway for terrestrial nutrients, carbon, metals, anthropogenic substances and persistent organic pollutants into the coastal ocean [*Burnett et al., 2001; Moore*, *2010*]. Discharge from unconfined near-shore aquifers to the ocean is a significant component of SGD, including discharges of fresh groundwater, recirculating seawater, and mixed salt and fresh-water. These discharges are dynamic processes, controlled by tidal fluctuations, wave set-up, storm events, winds, seasonal changes and density dependent flow along the saltwater-freshwater mixing zone [*Guo et al., 2009; Santos et al., 2012; Xin et al., 2015; Itugha et al., 2016*]. Saltwater-freshwater mixing processes have been proven to accelerate chemical flux from aquifers to the ocean, alter geochemical conditions, change habitat species and affect biogeochemical reactions in aquifers [*Slomp and Van Cappellen, 2004; Anschutz et al., 2009; Moore, 2010; Charbonnier et al., 2013*].

Saltwater-freshwater mixing in beach aquifers has long been thought to occur mainly in the salt wedge (see Figure 1) dispersion zone [*Cooper et al., 1964; Robinson et al., 2007a; Pool et al., 2014*]. However, integrated field salinity measurements [*Robinson et al., 1998; Urish and McKenna, 2004; Michael et al., 2005; Robinson et al., 2007b; Vandenbohede and Lebbe, 2006, 2007; Abarca et al., 2013; Hesis and Michael, 2014*] and electrical resistivity tomography profiles [*Turner and Acworth, 2004; Morrow et al., 2010; Befus et al., 2013; Buquet et al., 2016*] in intertidal regions, confirm the existence of another important mixing zone, the upper saline plume (USP) (see Figure 1), where saltwater-freshwater mixing is faster than that in the classical salt wedge. USP is an inverted structure with dense saltwater above light freshwater in shallow beach aquifers [*Ataie-Ashtiani et al., 1999; Boufadel, 2000; Mango er al., 2004*]. In the USP, pore-water has faster flow rates and significantly lower transit times than that in the dispersion zone of the classical salt wedge [*Robinson et al., 2007a*]. Therefore, this plume represents a potentially more dynamic zone for mixing and reaction than the salt wedge dispersion zone and may play a crucial role in geochemical transformation and coastal ecosystems [*Charette and Sholkovitz, 2002; Moore, 2010*].

Four essential conditions, namely, large enough oceanic oscillations, suitable terrestrial fresh groundwater flux, appropriate sloping intertidal topography, and moderate heterogeneity, are considered to be responsible for the formation of USP. Evans and Wilson [*2016*] noted that the development of an USP under a beach requires high rates of recirculation to create strong salinity gradients. This requires the infiltration of sufficient volumes of seawater into the beach aquifer and necessitates that the groundwater flush through the beach is not too rapid. Tides, which generate the main oceanic oscillations, have three main possible effects on saline recirculation in a beach: (i) tidal forcing making seawater intrude inland during flood phases and making brackish water percolate during ebb phases [*Nielsen, 1990; Li et al., 1997; Cartwright et al., 2004*]; (ii) widening the zone of dispersion [*Ataie-Ashtiani et al., 1999; Li et al., 2008; Kuan et al., 2012*]; and (iii) causing seawater to infiltrate into a beach directly from wave run-up [*Kang et al., 1995; Bakhtyar et al, 2013; Geng and Boufadel, 2015*]. The slope of a beach would intensify (e.g., a flatter slope) or weaken (e.g., a steeper slope) the infiltration of saltwater [*Ataie-Ashtiani et al., 1999; Li et al., 2008*]. High heterogeneity of a sloping beach will increase both the spatial connectivity and effective permeability in a porous beach to reduce the degree of mixing as well as the extent of USP [*Fiori and Jankovic, 2012*].

Tidal fluctuation will cause hydraulic head fluctuation and pore water salinity oscillation [*Erskine, 1991; Abdollahi-Nasab et al., 2010; Hesis and Michael, 2014; Elad et al., 2017*]. Tide-induced hydraulic gradients can result in a transient increase of the solute transfer rate more than 20 times higher than the average rate in the aquifers that undergo saltwater intrusion [*Li et al., 1999*] and likely contribute to fluctuations in submarine seepage rates [*Burnett et al., 2002*]. However, the transient behaviour of solute migration and the associated mixing processes under highly variable groundwater flow have remained largely unexplored so far. Several studies have been conducted to investigate some aspects of tidal fluctuations on the mixing patterns in shallow unconfined coastal aquifers. Numerical studies have concluded that salinity distribution does not fluctuate significantly over the tidal cycle [*Ataie-Ashtiani et al., 1999; Mao et al., 2006; Robinson et al., 2007a; Pool et al., 2014*]. However, the conceptual models suggest that the width of the freshwater discharge tunnel (FDT) contracts and expands over the semi-diurnal period [*Barry and Parlange, 2004*; *Urish and McKenna, 2004*], which is supported by laboratory experiments and field investigation [*Boufadel, 2000; Robinson et al., 2006, Shalev et al., 2009; Kuan et al., 2012, Abarca et al., 2013; Hesis and Michael, 2014*]. Such discrepancy shows that there still exists a knowledge gap for a full understanding of the behaviour of solute migration and the associated mixing processes under tide-dominated groundwater systems. Moreover, the magnitudes of mixing between seawater and fresh groundwater in the USP have not been properly quantified. This is partly due to the difficulties in measuring and quantifying the mixing process in groundwater systems under complex spatiotemporal flow variations. When tidal conditions include variable-density flows in a saturated-unsaturated aquifer with unpredictable seepage face, the strong non-linearity makes full understanding of the beach hydraulics a challenging task, even for spatially and temporally varying saltwater-freshwater mixing [*Bear, 1972; Simmons et al., 2001; Smith, 2004; Boufadel et al., 2011*]. The recently developed mesh-free numerical modelling technique, such as SPH [*Shao, 2012*], could be an effective method for simulating saltwater-freshwater mixing.

This study investigates the fluctuation of salinity distribution, examines whether the tidal driven force acts equally in the mixing behaviours at the upper saline plume and lower salt wedge, and explores the factors controlling the mixing fluctuation features, thus filling the knowledge gap in this field. To this end, we constructed variable-density, saturated-unsaturated, transient groundwater flow and solute transport models for a wide range of major hydrogeological parameters. The objectives of this study are (i) to evaluate the transient location and shape of the salinity distribution in the aquifer, considering tidal fluctuation effects, saturated-unsaturated flow and the seepage face developed at the aquifer-air interface and (ii) to further gain a quantitative understanding of the mixing behaviour under the above conditions, including the mixing pathway and mixing fluctuation characteristics. The results are analysed using a redefined spatial moment scheme for both the transient and the quasi-steady state to investigate the interaction between tidal fluctuations and mixing mechanisms.

2 Concepts and Methods

2.1 Problem Statement

A two-dimensional (2D) domain with a slope is set up to represent a cross-shore transect of an unconfined coastal aquifer with a length of L_x [L], a depth of L_y [L], a constant thickness of B [L] and a terrestrial freshwater flux of q_f [L^3 T^{-1} L^{-1}]. The beach slope with an angle θ is located at the upper part of the seaward boundary. The aquifer is assumed to be anisotropic and homogeneous. A Cartesian coordinate system is established with the x-axis pointing seaward orthogonally to the shoreline and the y-axis pointing vertically upward (see Figure 2).

2.2 Dimensional Analysis

The shallow coastal aquifer is parameterized for generic application as well as for better understanding the factors controlling seawater recirculation in the presence of tidal forcing. To this end, the aquifer depth B [L], vertical hydraulic conductivity K_V [L T^{-1}], freshwater density ρ_f [M L^{-3}], transverse dispersivity α_T [L] are used to normalize the key control parameters and the dimensionless parameters are defined as follows:

$$\delta = \frac{B}{A},\ q_f^* = \frac{BK_H}{q_f},\ K^* = \frac{K_H}{K_V},\ \rho^* = \frac{\rho_s - \rho_f}{\rho_f},\ \alpha^* = \frac{\alpha_L}{\alpha_T}\ ,\ D^* = \frac{B}{\alpha_T} \quad (1)$$

where δ is the tidal spatial ratio of the aquifer depth B relative to the tidal amplitude A [L], representing the strength of tidal forcing, q_f^* is the ratio of aquifer transmissivity ($K_H B$) to inland groundwater discharge flux, representing the inland hydraulic gradient, K^* is the ratio of horizontal hydraulic conductivity K_H to K_V, representing the anisotropy of the aquifer, ρ^* is the buoyancy factor, α^* is dispersivity anisotropy, and D^* is the dispersion parameter. The combination of δ, q_f^*, K^* and ρ^* controls the location and shape of the transition zone, while ρ^*, α^* and D^* control the rate of density-driven convection.

2.3 Numerical Methodology

In this study, the density-dependent variable-saturated groundwater flow and solute transport model SUTRA Version 2.2 [*Voss and Provost, 2010*] is employed to perform the numerical simulation. Though details of SUTRA 2.2 can be found in Voss and Provost [*2010*], a brief description of the model is provided here for completeness and convenience.

2.3.1 Governing equations

Neglecting subsidence and compaction, the model solves the *Richards* equation [*Richards, 1931*] with hydraulic conductivity for variable density groundwater flow. The governing equations for describing variable-density saturated-unsaturated groundwater flow are [*Voss and Provost,* 2010]

$$\frac{\partial(\varepsilon S_w \rho)}{\partial t} - \nabla \cdot [\rho k_r K \cdot \nabla h] = Q_p + \gamma \, , \tag{2}$$

$$h = h_p + ELEVATION \tag{3}$$

where ε [-] is the porosity of beach soil; S_w [-] is the sediment water saturation; ρ [M L^{-3}] is the fluid density; t [T] is time; k_r [-] is relative permeability to fluid flow; K [L s^{-1}] is the hydraulic conductivity; h [L] is the hydraulic head; h_p [L] is pressure head; Q_p [M L^{-3} s^{-1}] is fluid mass source term, accounting for external additions of fluid including pure water mass plus the mass of any solute dissolved in the source fluid; and γ [M L^{-3} s^{-1}] is the pure solute mass source term, accounting for external additions of pure mass not associated with a fluid source, e.g., dissolution of solid matrix or desorption.

The variable saturation can be described by the *van Genuchten* formulas [*van Genuchten, 1980; van Genuchten and Nielsen, 1985*].

$$S_w = 1, k_r = 1 \qquad \qquad saturated\ flow \tag{4}$$

$$k_r = {S_w^*}^{1/2} \left\{ 1 - \left[1 - {S_w^*}^{\left(\frac{n}{n-1}\right)} \right]^{\frac{n-1}{n}} \right\}^2 , \qquad unsaturated\ flow \tag{5}$$

$$S_w^* = \frac{S_w - S_{wres}}{1 - S_{wres}} = \frac{\theta_w - \theta_{wres}}{\theta_s - \theta_{wres}} = \left[\frac{1}{1 + (\alpha p_c/\rho g)^n}\right]^{\left(\frac{n-1}{n}\right)},$$

where S_{wres} [-] is residual saturation below which saturation is not expected to fall; S_w^* [-] is effective saturation; θ_w [-] is the volumetric water content; θ_s [-] is the saturated volumetric water content; θ_{wres} [-] is the residual volumetric water content; α [L^{-1}] is the capillary fringe parameter; n is the grain size distribution parameter; and p_c [$M\ L^{-1}\ s^{-2}$] is capillary pressure.

The solute transport model including advection, mechanical dispersion or molecular or ionic diffusion is described by

$$\frac{\partial(\varepsilon S_w \rho C)}{\partial t} = \nabla \cdot [S_w \rho K C \cdot \nabla h] + \nabla \cdot [\varepsilon S_w \rho (D + D_m I) \cdot \nabla C] + Q_p C^*, \quad (6)$$

where C [$M\ M^{-1}$] is dissolved solute concentration (mass fraction); D [$L^2\ s^{-1}$] is dispersion tensor; D_m [$L^2\ s^{-1}$] is apparent molecular diffusivity of solute in solution in a porous medium including tortuosity effects; I is identity tensor; and C^* [$M\ M^{-1}$] is solute concentration of fluid sources (mass fraction).

The relationship between fluid density ρ and the mass fraction C is calculated by using a linear equation, and assuming that only the salt mass fraction effect is considered:

$$\rho = \rho_0 + \frac{\partial \rho}{\partial C}(C - C_0), \quad (7)$$

where ρ_0 is the fluid density at a base salt mass fraction C_0, and $\partial\rho/\partial C$ is a constant coefficient of density variability due to a linearity assumption.

2.3.2 Boundary and initial conditions

We directly apply the tidal fluctuation at the seaward slope rather than introducing another zone as done by Robinson et al. [*2007a*]. A sinusoidal tidal fluctuation is implemented by applying temporal pressures or an equivalent freshwater head, $H(y, t)$, along the aquifer-ocean interface.

$$H(y,t) = h_{msl} + A\cos(2\pi t/\tau)\ , \tag{8}$$

where *H(y, t)* is the tidal level (L) at time *t*, h_{msl} is the mean sea level (set at 0 m), τ is the tidal period (T), and $\pi = 3.1415927$.

A seepage face boundary is introduced based on the approach presented by Park and Aral [*2008*] and Abdollahi-Nasab et al. [*2010*]. In other words, a Dirichlet boundary condition is set for the aquifer-ocean interface below the water level regardless if the flow enters or leaves the interface. The value of the pressure is set according to time-varying hydraulic heads and the salinity is equal to that in the seawater. No-flow and no dispersion flux boundary conditions are specified for the aquifer-ocean interface above the seepage face. The seaward vertical boundary is set as a no-flow boundary. The left boundary of the domain is set using a uniformly distributed constant flux, representing the fresh groundwater discharge into the domain. No water flow and solute transport occurs across the bottom boundary, considered as impermeable, i.e., $\partial h/\partial n = 0$ and $\partial c/\partial n = 0$. As precipitation and evapotranspiration are negligible, the upper boundary is set as an unsaturated free surface.

2.3.3 Numerical implementation

To quantify the effects of tides on solute mixing, models use a step-wise approach [*Robinson et al., 2007a*] in which models are initially run using a constant mean sea level at the seaward boundary until a steady state is reached. Tidal oscillations are then superimposed using the first-step results (i.e., salinity and hydraulic heads) as the initial condition and models are run until the dynamic quasi-steady state with respect to both heads and salinity is reached (i.e., the relative differences of hydraulic heads and salinity at the same cycle stage are within 1%). Simulations are performed by independently varying the tidal amplitude, the tidal period, the fresh groundwater flux, the hydraulic conductivity, the specific storage coefficient and the ratio of longitudinal and transverse dispersivities. Table 1 summarizes the range of parameters used in the numerical simulation performed in this study.

In different simulation scenarios, one parameter is systematically varied, while all others are held constant to examine the effect of this parameter on the simulation. The parameters for the base simulation are δ = 0.1, q_f^* = 0.01, K^* = 1, $\rho^* = 0.025$, α^* = 10 and D^* = 300. These values represent a typical tidally affected coastal aquifer system. In the vertical direction the model domain extends from 15 m below to 3 m above mean sea level. This aquifer depth is chosen to effectively perform the numerical computation and to ensure that D^* is realistic and does not create excessive backward dispersion across the aquifer-ocean interface.

SUTRA 2.2 is an unstructured grid model using a quadrilateral type of element. In the current study, a total of 37,000 quadrilateral elements and 37631 nodes are used for spatial discretization of the study area. Since the spatial discretization schemes play an important role in simulation accuracy, a non-uniform scheme is used and ensures a mesh Péclet number ($Pe_x = \Delta x/\alpha_L$, $Pe_y = \Delta y/\alpha_T$) less than 2 [*Voss and Souza, 1987*]. The horizontal grid-spacing ranges from 1 m in the most inland position to 0.5 m near the sloping beach and seaside boundaries. Finer grids (Δx = 1/3 m and Δy = 0.1 m) are used within the intertidal region where flow and mixing is stronger.

2.4 Quantification method

Previous studies using iso-salinity contours to demonstrate results only provide qualitative results showing the relative size and spread of the USP and salt wedge penetration. In this study, spatial moments of salt mass fractions are calculated to quantify the solute mixing and spreading processes. Four measurable parameters, namely, the centre of mass, the transverse mixing width and longitudinal mixing length, and the mixing volume, are used to demonstrate and quantify three key aspects of the problem under investigation, namely, the mass centre position of the mixing zone, the mixing range, and the accumulation of mixing. Though details for calculating these four parameters can be found in Pool et al. [*2014, 2015*], we present a brief description of their calculation here for convenience and completeness.

2.4.1 The mass centre position of the mixing zone

The mass centre position $(X_c, Y_c)(t)$ is defined by ratio of the zeroth and the first moments of the salinity distribution, $M^{(0)}(t)$ and $M^{(1)}(t)$, respectively,

$$X_c(t) = \frac{M_x^{(1)}(t)}{M^{(0)}(t)} \quad (9)$$

$$Y_c(t) = \frac{M_y^{(1)}(t)}{M^{(0)}(t)} \quad (10)$$

$$M^{(0)}(t) = \iint \omega(x,y,t)dxdy \quad (11)$$

$$M_x^{(1)}(t) = \iint \omega(x,y,t)xdxdy \quad (12)$$

$$M_y^{(1)}(t) = \iint \omega(x,y,t)ydxdy, \quad (13)$$

where subscript c indicates centre, subscript x indicates the horizontal direction, subscript y indicates the vertical direction, and ω is the salinity. Note that the location variance contains two points: one in the USP, the other in the SW.

2.4.2 The mixing range

Actual solute mixing is produced by the interaction of advectively created concentration contrasts and mass transfer due to diffusion. The mixing width needs to measure the increase of the extension of the mean concentration distribution and not the increase of the mean extension of the plume [*Dagan, 1988; Dentz et al., 2011*].

The mixing range is defined in horizontal and vertical directions using the rigorous method of Pool et al. [*2014, 2015*]. The longitudinal mixing length is derived by calculating the spatial moments of $g_x(x|y, t)$, which is defined by the scaled and normalized salinity distribution as following:

$$g_x(x|y,t) = \frac{\left[\omega(x,y,t) - \omega_f\right]\left[\omega_s - \omega(x,y,t)\right]}{\int\left[\omega(x,y,t) - \omega_f\right]\left[\omega_s - \omega(x,y,t)\right]dx}. \quad (14)$$

where ω_s is the seawater salinity, and ω_f is the inland groundwater salinity. The transverse mixing width is quantified by the spatial moments of $g_y(y|x, t)$, which can be defined similar to (14).

The spatial variance $\sigma^2_x(y, t)$ in the horizontal direction is derived from the first and second moments of $g_x(x|y, t)$,

$$\sigma_x^2(y,t) = \left\{m_x^{(2)}(y,t) - m_x^{(1)}(y,t)m_x^{(1)}(y,t)\right\} \tag{15}$$

$$m_x^{(1)}(y,t) = \int g_x(x|y,t)x dx \tag{16}$$

$$m_x^{(2)}(y,t) = \int g_x(x|y,t)x^2 dx. \tag{17}$$

The spatial variance $\sigma^2_y(x, t)$ in the vertical direction can be defined similarly to $\sigma^2_x(y, t)$. The longitudinal mixing length and the transverse mixing width of the transition zone are characterized by the standard deviations, $\sigma_x(y, t)$ and $\sigma_y(x, t)$, respectively. Because the transverse mixing width and the longitudinal mixing length are not constant along the interface, the averaged values, namely, $\langle\sigma_y\rangle(t)$ and $\langle\sigma_x\rangle(t)$, are calculated respectively along the vertical and horizontal directions of the mixing zone for both the USP and SW.

2.4.3 The accumulation of mixing

The accumulation of mixing is calculated using the mixing fluid volume. Based on the iso-salinity contour, the mixing volume $V_m(t)$ [L^3 L^{-1}] represents the mixing-zone volume per unit length of coastline bounded by a 0.1 (ω_{min}) and 0.9 (ω_{max}) normalized salinity contour line [*Pool et al., 2014*] and is defined as

$$V_m(t) = \int_V H[\omega(x,y,t) - \omega_{min}]H[\omega_{max} - \omega(x,y,t)]\varepsilon dx dy\,, \tag{18}$$

$$H(\omega) = \begin{cases} 1, & \omega \geq 0 \\ 0, & otherwise \end{cases} \tag{19}$$

where V is the bulk aquifer volume, and $H(\omega)$ is the Heaviside step function.

3 Results and discussions

3.1 Transient Behaviour

3.1.1 Qualitative analysis

Figure 3 displays the impact of tides on the temporal evolution of salt mass distribution. The simulations show that tidal forcing across the sloping beach surface can introduce the formation of USP, SW and FDT. Fresh groundwater discharge occurs through the tunnel between USP and SW. The saltwater-freshwater mixes little at the centre of the tunnel (which is apparent from the fact that salinity is still the same as freshwater at this position); however, at both tunnel sides, the mixing intensifies. A mixing gradient always points to the mass centre along the groundwater discharge pathway.

Tidal forcing can significantly affect the pattern of salinity distribution, including affecting the position where saltwater-freshwater mixing happens. In particular, the location and extent of the USP, the developing process of saltwater-freshwater interface and the transient behaviours of the salt wedge movement along the basement of aquifer are largely related to tidal forcing. Increase of the tidal amplitude can cause the USP to migrate deeper and wider, while the salt wedge movement towards the land is inhibited (see the 600 days results in the last line of Figure 3). This finding is consistent with the sand flume experiments of Kuan et al. [*2012*].

Under the action of tidal forcing, the equilibrium under constant mean sea level is broken as saltwater intrudes into the aquifer from the seaward boundary at the high tidal level. It is seen from Figure 3 that at the very early stage (e.g., the 1st day), the aquifer hydraulic head responds quickly, prior to the solute in the aquifer, to water level rising at the seaward boundary. The tide driven recirculation occurs faster than the density-driven recirculation. USP forms prior to the development of the salt wedge. Analysis of the simulation results reveals that the maximum Darcy velocity always appears at the intersection of the water table and the beach surface, while the offshore beach groundwater is almost stagnant compared with the onshore groundwater flow.

This asymmetry leads to a time-averaged groundwater circulation [*Mango et al., 2004*]. This confirms the previous finding of numerical work [*Ataie-Ashtiani et al., 1999; Boufadel, 2000; Mao et al., 2006; Robinson et al., 2007a; Li et al., 2008*] and sand flume experiments [*Kuan et al., 2012*].

Three different evolution patterns of DRZ can be identified by carefully examining the temporal evolution of the saline distributions for various tidal amplitudes. For a small tidal amplitude (e.g., A = 0.5 m), the DRZ begins to develop from the upper position of the aquifer rather than from the toe along the bottom. The infiltrated saline water into the aquifer first appears at the position below the low tidal mark, then gradually migrates downward. This migration enhances the salt wedge and makes it sufficiently strong to spread along the bottom to landward. Thus, the salt wedge first moves landwards at the shallow region then evolves into the deeper region. This dynamic may be ascribed to the fact that a small tidal amplitude does not have sufficient energy to affect the mixing behaviour deep in the aquifer. For a small tidal amplitude (e.g., A = 0.5 m), saltwater tends to intrude into the upper aquifer when water level rises to near high tidal level mark [*Vandenbohede and Lebbe, 2006; Robinson et al., 2007a, c; Abarca et al., 2013*].

In contrast, for a larger tidal amplitude (e.g., A = 1.0, 1.5 m), the development of DRZ is mainly restricted by the growth of the USP. For strong tidal forcing (i.e., a large tidal amplitude), the USP develops significantly and extends in both horizontal and vertical directions, which suppresses the spreading of the salt wedge at the middle to deep positions of the aquifer (see figures in the right column of Figure 3). This means that a higher tidal amplitude generates a deeper wide mixing layer. On the other hand, the large growth of the USP reduces the horizontal extent of the mixing at the upper part of the salt wedge. A crescent-shaped interface is formed after approximately 30 days of simulation. The simulation shows that the wide mixing at the middle position always passes downward to the bottom layer, causing salt to mix at bottom aquifer over the long term (e.g., over 300 days).

When the tidal amplitude increases to 2.0 metres, the development of DRZ seems to have the two above patterns. The simulation shows that the infiltration is dominant at the beginning (e.g., the first few days), then the USP pushing works at the later stage (e.g., after about one week). Though the infiltration dominates at the early stage for both the 0.5 m and 2.0 m tidal amplitude cases, the evolution processes are very different. As the USP grows much faster and larger for the 2-m tidal amplitude than that for the 0.5-m tidal amplitude case, the initial infiltrated saline water tends to mix quickly to form a wider mixing zone at the upper salt wedge for the larger tide. In other words, the quick development of the USP tends to intensify the mixing locally rather than push it into the deeper aquifer in the large tidal amplitude case. This demonstrates that a wider mixing zone develops in the upper aquifer for the large tidal amplitude. As a result, the position of the toe for large tidal amplitude is seaward, while it is landward for the smaller tidal amplitude. This suggests that the large tidal amplitude tends to develop the USP rather than the DRZ.

As the unsaturated part is included in the model, it allows us to investigate the coupling-decoupling processes at the saturated-unsaturated interface during the tidal flood and ebb phases. It is seen from the second row in Figure 3 (1 day figures) that saltwater diffuses into the aquifer when the saltwater level rises to near the high tidal level mark. The saltwater level then falls during the ebb phase while the decoupling process occurs. The water table slopes seaward during the ebb tide, some of the seawater that previously infiltrated the sediment progressively seeps out of the aquifer along the beach surface, while some remains at the unsaturated layer as residual water in the pore space. The maximum height of the seepage face always appears when the sea level reaches its lowest level. Figure 3 also shows that as the USP develops downwards, the mixing of plume fluid and fresh groundwater flow fluid occurs at its interface. The mixing event dilutes the plume fluid at its boundary layer (as seen in Figure 3), generating stratification within the USP.

The local salinity gradients provide direct evidence that saltwater-freshwater mixing occurs in both the USP and SW. The temporal evolution shows that the salinity distribution is a balance between the USP and SW. The growth of the USP makes the FDT move along the beach face towards the seaside. The width of the FDT gradually shrinks and then contracts and expands over the semi-diurnal period for all four tidal range cases (see Figure 3). This is in agreement with previous conceptual models [*Urish and McKenna, 2004*], but the USP does not vanish with the ebb tide, which accords with the previous numerical models [*Ataie-Ashtiani et al., 1999; Mao et al., 2006; Robinson et al., 2007a*]. This can be explained by the phase-averaged effect of tides, which can also be considered as an accumulative mass transport and storage effect.

3.1.2 Quantitative analysis

The above qualitative analysis shows the different evolution patterns of salinity distribution corresponding to various tidal amplitudes. This section will conduct quantitative investigation to further understand the problem under study. The temporal behaviours of mass centre position and the mixing range are extracted from the simulation results to characterize the problem under the action of four tidal amplitudes.

Figure 4 is the temporal variation of the mass centre of the USP and DRZ. Different stages of the centre migration are seen in the transient state. In general, the mass centre of the USP has a sharp movement downwards and towards offshore except the case of small tidal forcing (e.g., A = 0.5 m), in which the mass centre movement is gradual in both directions throughout the computational period. After a short transition, the position of the mass centre of the USP oscillates horizontally and vertically around an asymptotic value at approximately 30 days (see also Figure 3), indicating that a periodic quasi-steady state is reached. Figure 4 also shows that the highest tidal amplitude generates the lowest position of the mass centre of the USP. This may be ascribed to the fact that the density and size of the USP generated by a large tide is larger than that generated by a small tide (see also Figure 3).

On the other hand, the movement of the mass centre of the DRZ shows a different evolution pattern. A sharp onshore and downwards movement of the mass centre is seen to occur at the early stage. When the mass centre of the DRZ reaches the lowest vertical position, it bounces back to stabilize a little above its lowest position. The movement of the mass centre of the DRZ in the horizontal direction slightly differs from its vertical movement. After the mass centre reaches the furthest onshore position at approximately 100 days, there is little horizontal and vertical movement observed for the mass centre. Figure 4 also demonstrates that the vertical movement of the mass centre of the DRZ is much smaller than its horizontal movement. It is seen that the vertical height of the mass centre of the DRZ decreases with the increase of the tidal amplitude, while the horizontal onshore position of the mass centre of the DRZ increases with the decrease of the tidal amplitude.

Unlike the oscillation feature of the mass centre of the USP, the mass centre of the DRZ does not have significant fluctuation around its asymptotic value after it reaches this asymptotic value. The time lag between the USP and DRZ to reach the asymptotic value is approximately 90 days. This result implies that the energy to maintain the tidal fluctuation is mostly passed to the USP rather than to the DRZ when considering beach morphology with a slope.

Figure 5 displays the transient behaviour of the transverse mixing width and the longitudinal mixing length in the USP and DRZ, respectively. A sharp increase of the transverse mixing width and longitudinal mixing length of the USP is seen to occur, although the extent of the increase largely depends on the tidal forcing. This sharp increase reaches its maximum at approximately 30 days, and then, a quasi-steady state is reached for all the tidal amplitudes simulated. This finding is consistent with the results shown in Figures 3 and 4. Figures 5a and 5c show that both the transverse mixing width and longitudinal mixing length of the USP increases with the increase of the tidal amplitude. This is because the USP generated by a larger tidal amplitude has a larger initial potential energy and hydrostatic pressure which in turn generates a larger penetration velocity (see the slope of $\langle\sigma_y\rangle(t)$ and $\langle\sigma_x\rangle(t)$ in Figures 5a and 5c). The higher velocity generates strong mixing, resulting in a wider and deeper mixing zone. It is also seen that the longitudinal mixing length is approximately 4 times the transverse mixing width, indicating that the mixing of the USP mainly occurs in the horizontal direction. This finding agrees with that by Boufadel et al. [*2011*] who found that dispersivity did not affect the travel time of the peak of solute concentration at a specific location but did affect its magnitude.

Similarly, Figures 5b and 5d show that an initial very short oscillation for both the transverse mixing width and longitudinal mixing length of the DRZ exists. A sharp increase of the transverse mixing width and the longitudinal mixing length occurs before a quasi-steady state is reached. Unlike the USP, the time for reaching a quasi-steady state depends on the tidal forcing. The larger the tidal amplitude, the shorter the time required for the transverse mixing width and the longitudinal mixing length of the DRZ to reach the steady state.

Before the quasi-steady state is reached, as expected, the tidal fluctuation mainly exhibits in the USP rather than in the DRZ, except in the case of A = 0.5 m. Unlike the transient behaviour of the mass of centre, the temporal evolution of the transverse mixing width for the A = 0.5 m case shows appreciable oscillation to reach the quasi-steady state. This can be explained by the transient evolution discussed in Figure 3 in which the slow development of the USP leads to a periodic saltwater intrusion into the shallow aquifer from the upper DRZ which itself has the feature of tidal oscillation. On the other hand, a small USP causes significant unbalance from landward to neutralize the periodic oscillation at the seaward boundary, making the DRZ partially oscillate with the tidal fluctuation.

Figures 5b and 5d also show a different increase pattern comparing with the USP. Both the transverse mixing width and longitudinal mixing length of the DRZ increases with the decrease of the tidal amplitude (see also the fourth line of Figure 3, 600 days). This can be explained as follows. A small tidal amplitude makes the DRZ migrate longer a distance landward than the larger tidal amplitude does. This is because a longer and broader USP generated by large tidal forcing develops from a sloped beach and tends to suppress the DRZ evolution landwards. In addition, a smaller tidal amplitude (e.g., A = 0.5 m) causes a more seawards USP than a larger tidal amplitude (e.g., A = 2.0 m).

Another quantitative parameter to describe the mixing event is the mixing volume, which represents the accumulation of mixing fluid in the aquifer. Figure 6 shows the temporal evolution of the mixing volume. It is seen that the development of the mixing fluid volume sharply increases with time at the early stage and then reaches a quasi-steady state at 70 days for the USP (Figure 6a) and 130 days for the DRZ (Figure 6b). The mixing fluid volume of the USP significantly increases with the increase of the amplitude of the tidal forcing. Simulation shows that the mixing fluid volume at the quasi-steady state for A = 2.0 m is approximately 45 times that for A = 0.5 m. Figure 6 reveals that the mixing fluid volume of the DRZ decreases slightly with an increase of the tidal amplitude, indicating that the effect of the tidal forcing on the DRZ is marginal.

3.2 Steady State Behaviour

Previous studies suggest that once the quasi-steady state is reached, the salinity distribution in coastal aquifers will not fluctuate significantly over a tidal cycle [see, e.g., *Ataie-Ashtiani et al., 1999; Dentz and Carrera, 2003; Pool et al., 2014*]. The results obtained from this study show that behaviour of mass centre position, mixing width and length, and mixing volume of the DRZ, but not those of the USP, agree well with previous studies. These findings imply that there may exist another mechanism that governs the migration of the salt mass and the mixing behaviour of the USP when a quasi-steady state is reached. To further investigate this, the mass centre position and the mixing behaviour around its mean position over a daily cycle are analysed for the quasi-steady state.

Figure 7 illustrates the temporal variation of centre of mass around its mean position $(\overline{X}_c, \overline{Y}_c)$ over two tidal cycles (t = 24 h) once the quasi-steady state is reached. It is seen that the fluctuation amplitude of the mass centre in the USP increases with increase of tidal amplitude. In particular, when tidal amplitude increases from 0.5 m to 1.0 m, the fluctuation extent increases almost 5 times. When tidal amplitude continues to increase (e.g., from 1.0 m to 2.0 m), the increase of fluctuation becomes gradual, e.g., the fluctuation response to an increase of tidal amplitude from 1.0 m to 2.0 m is only 1/5. Figures 7a and 7c also demonstrate that there is no significant phase lag of vertical mass centre oscillation between tidal signal and USP oscillation, while more than a $5\pi/4$ phase lag is observed for horizontal component of mass centre of the USP for tidal amplitude increases from 1.0 m to 2.0 m. It is evident that the phase-resolved effect of tides is more significant for salt transport in horizontal directions of aquifers. Furthermore, for all four tidal cases, tidal fluctuations cause the horizontal component of the mass centre of the USP to be more displaced back than forth around its mean position. For the vertical component, it becomes more up than down. That is, for both components, the behaviour of the mass centre is asymmetric.

The fluctuation of both the horizontal and vertical mass centres of the DRZ around its mean location is very small (see also Figure 4), indicating that a very steady state for the mass centre of the DRZ is reached. However, the phase lag needs to be mentioned, for the horizontal component of the mass centre of the DRZ (see Figure 7b) there is almost a $\pi/2$ phase difference between tidal signal and DRZ oscillation. For the vertical component of the mass centre of the DRZ (see Figure 7d), the situation becomes complicated; four different tidal amplitudes cause four kinds of responses (see Figure 7d). This finding implies that the tidal effect on the evolution of the vertical component of the DRZ is complex.

Figure 8 shows the oscillation of the mixing width and length is around its averaged value when a quasi-steady state is reached. For the transverse mixing width of the USP, there is almost no phase lag at the first half tidal cycle, while phase lag is seen at the other half tidal cycle (see Figure 8a), which seems to increase with the increase of tidal amplitude. For a small tidal amplitude (e.g., A = 0.5 m), two peak values for the longitudinal mixing length of the USP exist over a tidal cycle, and they occur roughly at the highest and lowest tidal levels for the 1.0 m case, and both occur at the highest tidal level for the 0.5 m case. This phenomenon is also observed in the study assuming a vertical beach face [*Pool et al., 2014*], which supposed the phenomenon was attributable to the unsynchronized movement between the saline end and the freshwater end of the mixing zone. On the other hand, for larger tidal amplitudes, the longitudinal mixing length of the USP behaves normally, only displaying an increase of phase lag with an increase of tidal amplitude. The asymmetric oscillation still exists for both the transverse mixing width and the longitudinal mixing length of the USP (see Figures 8a, 8c).

The fluctuation of both the transverse mixing width and longitudinal length of the DRZ around its mean value $\overline{\langle\sigma\rangle}$ is very small (see also Figure 5) and it may be concluded that a very steady state for the transverse mixing width and longitudinal length of the DRZ is reached.

Comparing the transverse mixing width to the longitudinal mixing length of the USP and DRZ demonstrates that the temporal variations of flow at the seaward boundary enhance longitudinal dispersivity as well as transverse dispersivity in the USP, while effects on both longitudinal dispersivity and transverse dispersivity of the DRZ are small.

Figure 9 shows the tidal influence on the mixing volume of the USP and the DRZ in a daily cycle. The results show that a large mixing fluid volume oscillation around its averaged value exists for the USP, while insignificant oscillation of the mixing fluid volume of the DRZ around its mean value is observed after the quasi-steady state is reached. The mixing volume oscillation amplitude of the USP is more than 10 times that of the DRZ. This implies that the tide not only accelerates the formation of the USP but also maintains its fluctuation around a relative constant value when a quasi-steady state is reached.

To examine the relative importance of different parameters, the fluctuation amplitude of the mass centre, mixing width and length, and mixing volume are calculated under six dimensionless parameters. To avoid repetition, here, we only show the results of the fluctuation amplitude of longitudinal mixing length and the transverse mixing width. As shown in Figure 10, the fluctuation amplitude of both the longitudinal mixing length and the transverse mixing width in the USP are at least one order magnitude larger than those in the DRZ. This finding again emphasizes that the USP is the dominant mixing region in tidally dominated beach aquifers with a sloping beach face.

There are differences when comparing six different dimensionless parameters. In the transverse direction (see Figure 10c), the strength of tidal forcing and the slope of the beach can change the fluctuation amplitude of mixing. The remaining four parameters rarely have any contribution to the fluctuation of the transverse mixing width. The fluctuation amplitude of the transverse mixing width in the intertidal zone increases with the increase of the beach slope. The simulation shows that such fluctuation amplitude for the steep slope (e.g., beach slope = 0.3) is approximately 50% larger than that of the mild slope beach (e.g., beach slope = 0.1). In the longitudinal direction (see Figure 10a), the strength of tidal forcing, the inland hydraulic gradient, hydraulic conductivity and the slope of the beach collectively control the fluctuation amplitude. A steep slope tends to decrease the fluctuation amplitude of the longitudinal mixing length. This is because the steep beach face is too high to prevent strong salinity gradients from developing [*Evans and Wilson, 2016*]. The anisotropy of hydraulic conductivity is a finite regulator to adjust the amplitude of mixing on the basis of tidal oscillation. It is interesting to note that when the anisotropy of dispersivity is small (e.g., $\alpha_L/\alpha_T < 5$), the aquifer cannot prevent seawater intrusion but can eliminate the fluctuation of the longitudinal mixing length.

4 Conclusion

Saltwater-freshwater mixing in the near shore region is significant for chemical fluxes from the aquifer to the ocean. The upper saline plume in the intertidal region has proven to be a more active zone for mixing and reaction than the classical salt wedge. This study examines tidal effects on saltwater-freshwater mixing fluctuations in unconfined coastal aquifers using two-dimensional numerical models for a wide range of hydrogeological parameters. The mixing characteristics of the USP and DRZ are investigated and quantified using three measurable parameters to quantify three aspects of the problem under investigation, namely, the mass centre position of the plume, the mixing range, and the accumulation of mixing. The effect of tidally driven dynamic circulation on the mixing and spreading behaviour of the USP and the DRZ has been investigated and discussed.

Results suggest that tidal forcing can greatly affect the USP yet has an insignificant effect on the DRZ. The tidal amplitude not only affects the saline plume size but also affects the process of the plume reaching a quasi-steady state. The results clearly demonstrate that an increase in the tidal amplitude causes the mass centre of the USP to spread deeper and wider, as well as inhibits the mass centre of the DRZ from moving further into the land. Furthermore, tidal forcing causes an increase of both the transverse mixing width and longitudinal mixing length of the USP. In contrast, an increase of the tidal amplitude decreases the growth of the transverse mixing width and longitudinal mixing length of the DRZ. The fluctuation amplitude of the mass centre, mixing width and length, and mixing volume in the USP are, in general, one-magnitude-order larger than those in the DRZ.

The mixing in the USP largely inherits the fluctuation characteristics of tides in both transverse and longitudinal directions. Meanwhile, the mixing in the DRZ is relatively steady and shows little fluctuation. The effect of beach slope on mixing in the USP is reversed in the longitudinal and transverse directions. A steep slope tends to promote mixing fluctuation in the transverse direction and suppress mixing oscillation in the longitudinal direction.

This study has only examined the impact of sinusoidal fluctuations of the sea level on the salt mass spreading, mixing and quasi-steady distributions in shallow unconfined coastal aquifers. However, real tides have multiple harmonic constituent signals and long time scale variability leading to various flow patterns and instabilities that will induce significant variations in the intertidal salinity structure [*Robinson et al., 2007b; Abarca et al., 2013; Hesis and Michael, 2014*]. Further study is required to take into account time scales, dynamic spatial distributions, and the frequency and amplitude of mixing fluctuation to simulate the actual situation under real tides.

Acknowledgements

The research reported here was financially supported by the Shenzhen Key Laboratory for Coastal Ocean Dynamics and Environment (No. ZDSY20130402163735964), National High Technology Research & Development Program of China (No. 2012AA09A409). Comments and suggestions made by reviewers have greatly improved the quality of the final paper.

References

Abarca, E., H. Karam, H. F. Hemond, C. F. Harvey (2013) Transient groundwater dynamics in a coastal aquifer: the effects of tides, the lunar cycle, and the beach profile, Water Resour. Res., 49, 2473-2488.

Abdollahi-Nasab, A., M. C. Boufadel, H. Li, J. W. Weaver (2010), Saltwater flushing by freshwater in a laboratory beach, J. Hydrol., 386, 1-12.

Anschutz, P., T. Smith, A. Mouret, J. Deborde, S. Bujan, P. Poirier, and P. Lecroart (2009), Tidal sands as biogeochemical reactors, Estuarine Coastal Shelf Sci., 84, 84–90.

Ataie-Ashtiani, B., R. E. Volker, and D. A. Lockington (1999), Tidal effects on sea water intrusion in unconfined aquifers, J. Hydrol., 216, 17–31.

Bakhtyar, R., A. Brovelli, D. A. Barry, C. Robinson, L. Li (2013), Transport of variable-density solute plumes in beach aquifers in response to oceanic forcing, Adv. Water Resour., 53, 208-224.

Barry, D. A., J. Y. Parlange (2004), Subsurface pathways of contaminants to coastal waters, Advances in Hydro-Science and Engineering, 6, 525-526.

Bear, J. (1972), Dynamics of fluids in porous media, 764 pp., American Elsevier.

Befus, K. M., M. B. Cardenas, D. V. Erler, I. R. Santos, B. D. Eyre (2013), Heat transport dynamics at sandy intertidal zone, Water Resour. Res., 49, 3770-3786.

Boufadel, M. C. (2000), A mechanistic study of nonlinear solute transport in a groundwater-surface water system under steady state and transient hydraulic conditions, Water Resour. Res., 36, 2549–2565.

Boufadel, M. C., Y. Xia, and H. Li (2011), Modeling solute transport and transient seepage in a laboratory beach under tidal influence, Environ. Modell. Software, 26, 899-912.

Buquet, D., C. Sirieix, P. Anschutz, P. Malaurent, C. Charbonnier, F. Naessens, S. Bujan, P. Lecroart (2016), Shape of the shallow aquifer at the fresh water-sea water interface on a high-energy sandy beach, Estuarine Coastal Shelf Sci., 179, 79-89.

Burnett, B., J. Chanton, J. Christoff, E. Kontar, S. Krupa, M. Lambert, W. Moore, D. O'Rourke, R. Paulsen, C. Smith, L. Smith, M. Taniguchi (2002), Assessing methodologies for measuring groundwater discharge to the ocean, EOS, Transactions American Geophysical Union 83, 117-123.

Burnett, W. C., M. Taniguchi, J. Oberdorfer (2001), Measurement and significance of the direct discharge of groundwater into the coastal zone, J. Sea Res., 46, 109-116.

Cartwright, N., P. Nielsen, L. Li (2004), Experimental observations of watertable waves in an unconfined aquifer with a sloping boundary, Adv. Water Resour., 27, 991-1004.

Charbonnier, C., P. Anschutz, D. Poirier, S. Bujan, P. Lecroart (2013), Aerobic respiration in a high-energy sandy beach, Mar. Chem., 155, 10-21.

Charette, M. A., and E. R. Sholkovitz (2002), Oxidative precipitation of groundwater-derived ferrous iron in the subterranean estuary of a coastal bay, Geophys. Res. Lett., 29, 1-4.

Cooper, H. H. Jr., F. A. Kohout, H. R. Henry, R. E. Glover (1964), Sea water in coastal aquifers, U. S. Geological Survey Water-Supply Paper 1613-C.

Dagan, G. (1988), Time-dependent macrodispersion for solute transport in anisotropic heterogeneous aquifers. Water Resour. Res., 24, 1491-1500.

Dentz, M., and J. Carrera (2003), Effective dispersion in temporally fluctuating flow through a heterogeneous medium, Phys. Rev. E, 68, 036310.

Dentz, M., T. Le Borgne, A. Englert, B. Bijeljic (2011), Mixing, spreading and reaction in heterogeneous media: A brief review, J. Contam. Hydrol., 120-121, 1-17.

Elad, L., Y. Yoseph, G. Haim, S. Eyal (2017), Tide-induced fluctuations of salinity and groundwater level in unconfined aquifers – Field measurements and numerical model, J. Hydrol., 551, 665-675.

Erskine, A. D. (1991), The effect of tidal fluctuation on a coastal aquifer in the UK, Groundwater, 29, 556-562.

Evans, T. B., and A. M. Wilson (2016), Groundwater transport and the freshwater-saltwater interface below sandy beaches, J. Hydrol., 538, 563-573.

Fiori, A., and I. Jankovic (2012), On preferntial flow, channeling and connectivity in heterogeneous porous formations, Math. Geosci., 44, 133-145.

Geng, X., and M. C. Boufadel (2015), Numerical study of solute transport in shallow beach aquifers subjected to waves and tides, J. Geophys. Res. Oceans, 120, 1409-1428.

Guo, Y. K., J. S. Zhang, L. X. Zhang, Y. M. Shen (2009), Computational investigation of typhoon-induced storm surge in the Hangzhou Bay, China. Estuarine Coastal Shelf Sci., 85, 530-537.

Heiss, J. W., and H. A. Michael (2014), Saltwater-freshwater mixing dynamics in a sandy beach aquifer over tidal, spring-neap, and seasonal cycles, Water Resour. Res., 50, 6747-6766.

Itugha, O. D., D. Y. Chen, Y. K. Guo (2016), Pollutant advestive spreading in beach sand exposed to high-energy tides, Estuarine Coastal Shelf Sci.,181, 70-82.

Kang, H. Y., P. Nielsen and D. J. Hanslow (1995), Watertable overheight due to wave runup on a sandy beach, Coast. Eng., 1994, 2115-2124.

Kuan, W. K., G. Jin, P. Xin, C. Robinson, B. Gibbes, and L. Li (2012), Tidal influence on seawater intrusion in unconfined coastal aquifers, Water Resour. Res., 48, W02502.

Li, L., D. A. Barry, C. B. Pattiaratchi (1997), Numerical modelling of tide-induced beach water table fluctuations, Coast. Eng., 30, 105-123.

Li, L., D. A. Barry, F. Stagnitti, J. Y. Parlange (1999), Submarine groundwater discharge and associated chemical input to a coastal sea, Water Resour. Res., 35, 3253-3259.

Li, H., M. C. Boufadel and J. Weaver (2008), Tide-induced seawater-groundwater circulation in shallow beach aquifers, J. Hydrol., 352, 211–224.

Mango, A. J., M. W. Schmeeckle, D. J. Furbish (2004), Tidally induced groundwater circulation in an unconfined coastal aquifer modeled with a Hele-Shaw cell, Geology, 32, 233-236.

Mao, X., P. Enot, D. A. Barry, L. Li, A. Binley, D. S. Jeng (2006), Tidal influence on behaviour of a coastal aquifer adjacent to a low-relief estuary, J. Hydrol., 327, 110-127.

Michael, H. A., A. E. Mulligan, C. F. Harvey (2005), Seasonal oscillations in water exchange between aquifers and the coastal ocean, Nature, 436, 1145-1148.

Moore, W. S. (2010), The effect of submarine groundwater discharge on the ocean, Annu. Rev. Mater. Sci., 2, 59–88.

Morrow F. J., M. R. Ingham, and J. A. McConchie (2010), Monitoring of tidal influences on the saline interface using resistivity traversing and cross-borehole resistivity tomography, J. Hydrol., 389, 69-77.

Nielsen, P. (1990), Tidal dynamics of the water table in beaches, Water Resour. Res., 26, 2127–2134.

Park C. H. and M. M. Aral (2008), Salwater intrusion hydrodynamics in a tidal aquifer, J. Hydrol. Eng. , 13, 863-872.

Pool, M., V. E. A. Post, and C. T. Simmons (2014), Effects of tidal fluctuations on mixing and spreading in coastal aquifers: Homogeneous case, Water Resour. Res., 50, 6910-6926.

Pool, M., V. E. A. Post, and C. T. Simmons (2015), Effects of tidal fluctuations and spatial heterogeneity on mixing and spreading in spatially heterogeneous coastal aquifers, Water Resour. Res., 51, 1570-1585.

Richards, L. A. (1931), Capillary conduction of liquids through porous mediums, Physics, 1, 318.

Robinson, M. A., D. Gallagher, and W. Reay (1998), Field observations of tidal and seasonal variations in ground water discharge to tidal estuarine surface water, Ground Water Monitoring & Remediation, 18, 83-92.

Robinson, C., B. Gibbes, and L. Li (2006), Driving mechanisms for groundwater flow and salt transport in a subterranean estuary, Geophys. Res. Lett., 33, 155-170.

Robinson, C., L. Li, and D. A. Barry (2007a), Effect of tidal forcing on a subterranean estuary, Adv. Water Resour., 30, 851-865.

Robinson, C., B. Gibbes, H. Carey, and L. Li (2007b), Salt-freshwater dynamics in a subterranean estuary over a spring-neap tidal cycle, J. Geophys. Res., 112, 766-776.

Robinson, C., L. Li, and H. Prommer (2007c), Tide-induced recirculation across the aquifer-ocean interface, Water Resour. Res., 43, W07428, doi:10.1029/2006WR005679.

Santos, I. R., B. D. Eyre, M. Huettel (2012), The driving forces of porewater and groundwater flow in permeable coastal sediments: A review, Estuarine Coastal Shelf Sci., 98, 1-15.

Shalev, E., A. Lazar, S. Wollman, S. Kington, Y. Yechieli, H. Gvirtzman (2009), Biased monitoring of fresh water-salt water mixing zone in coastal aquifers, Groundwater, 47, 49-56.

Shao, S. (2012), Incompressible smoothed particle hydrodynamics simulation of multifluid flows, Int. J. Numer. Meth. Fluid, 69, 1715-1735.

Simmons, C. T., T. R. Fenstemaker, and J. M. Sharp Jr. (2001), Variable-density groundwater flow and solute transport in heterogeneous porous media: Approaches, resolutions and future challenges, J. Contam. Hydrol., 52, 245–275.

Slomp, C., P. Van Cappellen (2004), Nutrient inputs to the coastal ocean through submarine groundwater discharge: controls and potential impact, J. Hydrol., 295, 64-86.

Smith, A. J. (2004), Mixed convection and density-denpendent seawater circulation in coastal aquifers, Water Resour. Res., 40, 474-480.

Turner I. L., and R. I. Acworth (2004), Field measurements of beachface salinity structure using cross-borehole resistivity imaging, J. Coastal Res., 20(3), 753-760.

Urish, D. W., and T. E. McKenna (2004), Tidal effects on ground water discharge through a sandy marine beach, Groundwater, 42(7), 971–982.

van Genuchten, M. T. (1980), A Closed-form Equation for Predicting the Hydraulic Conductivity of Unsaturated Soils, Soil Sci. Soc. Am. J., 44, 892-898.

van Genuchten, M. T., D. R. Nielsen (1985), On describing and predicting the hydraulic properties of unsaturated soils, Ann. Geophys., 3, 615-628.

Vandenbohede, A., and L. Lebbe (2006), Occurence of salt water above fresh water in dynamic equilibrium in a coastal groundwater flow system near De Panne, Belgium, Hydrogeol. J., 14, 462–472.

Vandenbohede, A., and L. Lebbe (2007), Effects of tides on a sloping shore: groundwater dynamics and propagation of the tidal wave, Hydrogeol. J., 15, 645-658.

Voss, C. I., and A. M. Provost (2010), A model for saturated-unsaturated, variable-density ground-water flow with solute or energy transport, *Rep.*, U.S. Geological Survey, Reston, Virginia, Report 02-4231.

Voss, C. I., and W. R. Souza (1987), Varable density flow and solute transport simulation of regional aquifers containing a narrow freshwater-saltwater transition zone, Water Resour. Res., 23, 1851-1866.

Xin, P., S. S. J. Wang, C. Lu, C. Robinson, and L. Li (2015), Nonlinear interactions of waves and tides in a subterranean estuary, Geophys. Res. Lett., 42, 2277-2284.

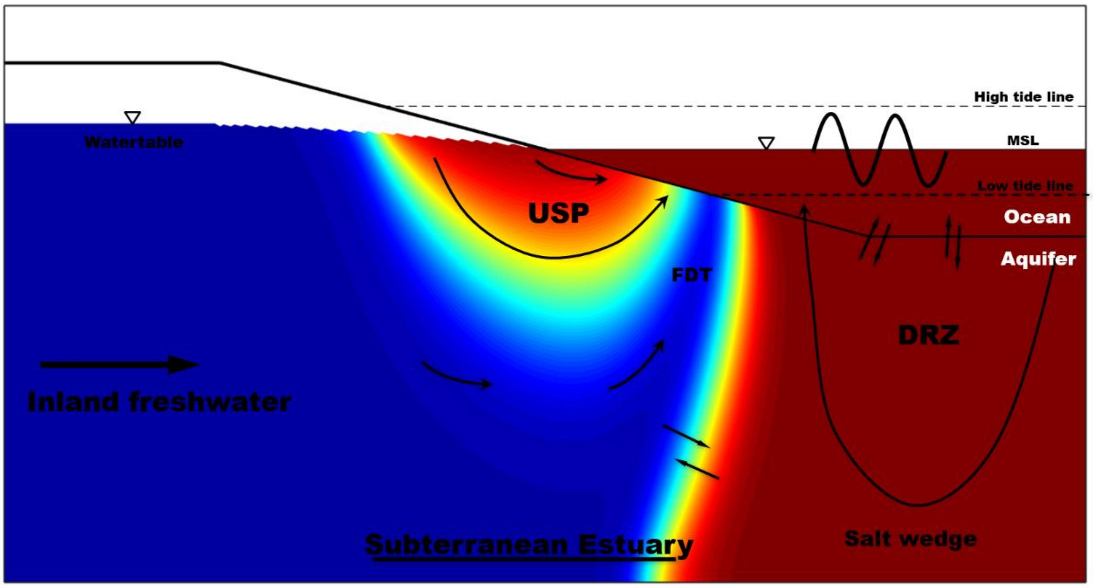

Figure 1. Conceptual diagram of subterranean estuary including major nearshore circulations. Showing upper saline plume (USP), freshwater discharge tube (FDT), salt wedge (SW) and density driven recirculation zone (DRZ).

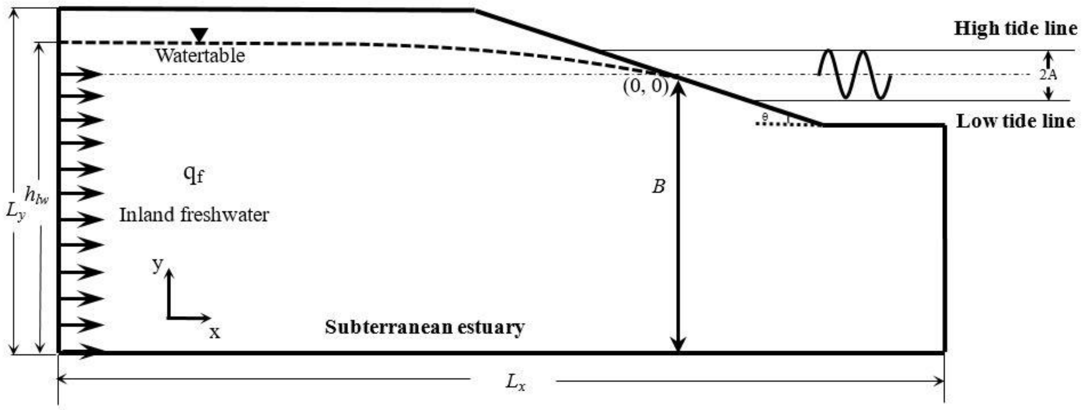

Figure 2. Sketch of the model geometry (2-D vertical cross-section) and boundary conditions. The dashed line represents the beach watertable, and the dash-dot line represents the mean sea level (MSL).

Table 1. Parameters Used in Numerical Simulations

Symbol	Parameter	value
K_H	Hydraulic conductivity [m d^{-1}]	7.6-152.6
S_s	Specific storativity [m^{-1}]	7.36×10^{-2}
q_f	Terrestrial fresh groundwater flux [m^3 d^{-1} m^{-1} shoreline]	0-4.0
ε	Effective porosity [-]	0.25
B	Aquifer thickness [m]	15
S_b	Beach slope [-]	0.1
α_L	Longitudinal dispersivity [m]	0.5
α_T	Transverse dispersivity [m]	0.005-0.5
ρ_f	Freshwater density [kg m^{-3}]	1000
ρ_s	Seawater density [kg m^{-3}]	1024.99
D_m	Molecular diffusivity [m^2 s^{-1}]	1.0×10^{-9}
μ	Fluid viscosity [kg m^{-1} s^{-1}]	0.001
S_{wres}	Residual saturation [-]	0.2
α	Van Genuchten capillary fringe parameter [m^{-1}]	0.8
n	Van Genuchten grain size distribution parameter [-]	3.0
A	Tidal amplitude [m]	0.5-2.0
τ	Tidal period [d]	0.5

* values in parentheses with hyphens are the minimum and maximum.

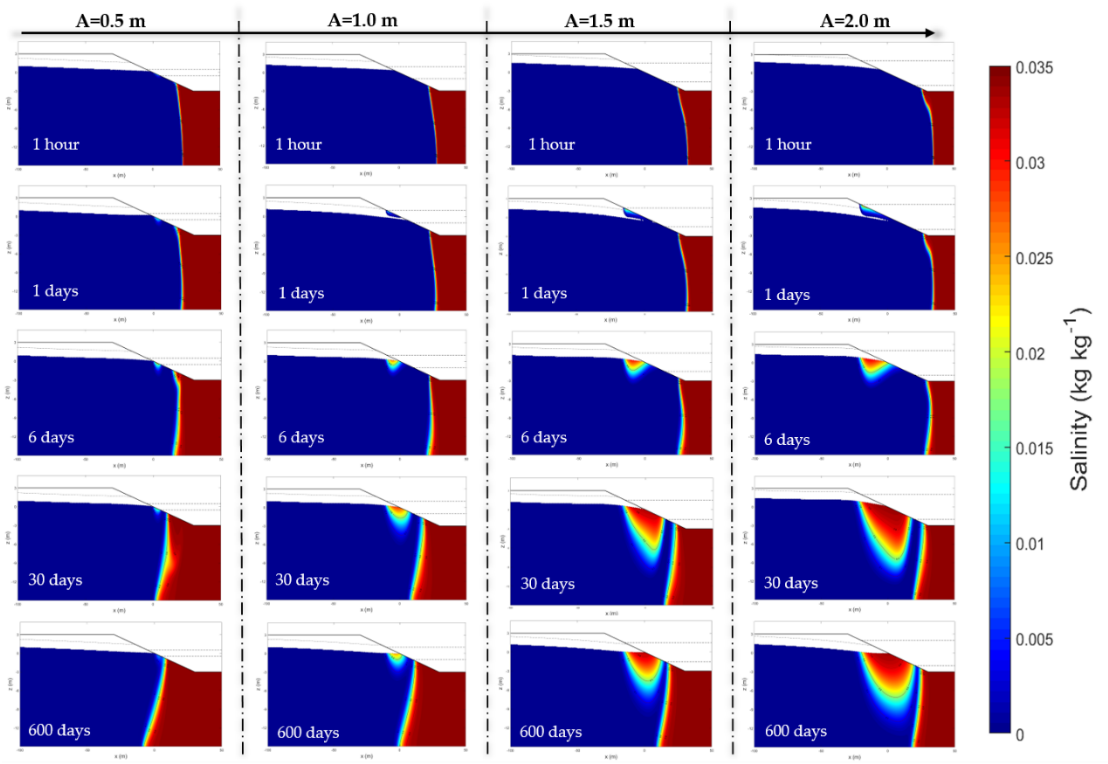

Figure 3. Temporal evolution of the saline distributions for various tidal amplitudes, showing the USP and DRZ growing processes, and the distinct coupling-decoupling of saturated-unsaturated layer. Two parallel dashed lines at the seaward boundary represent the tidal range.

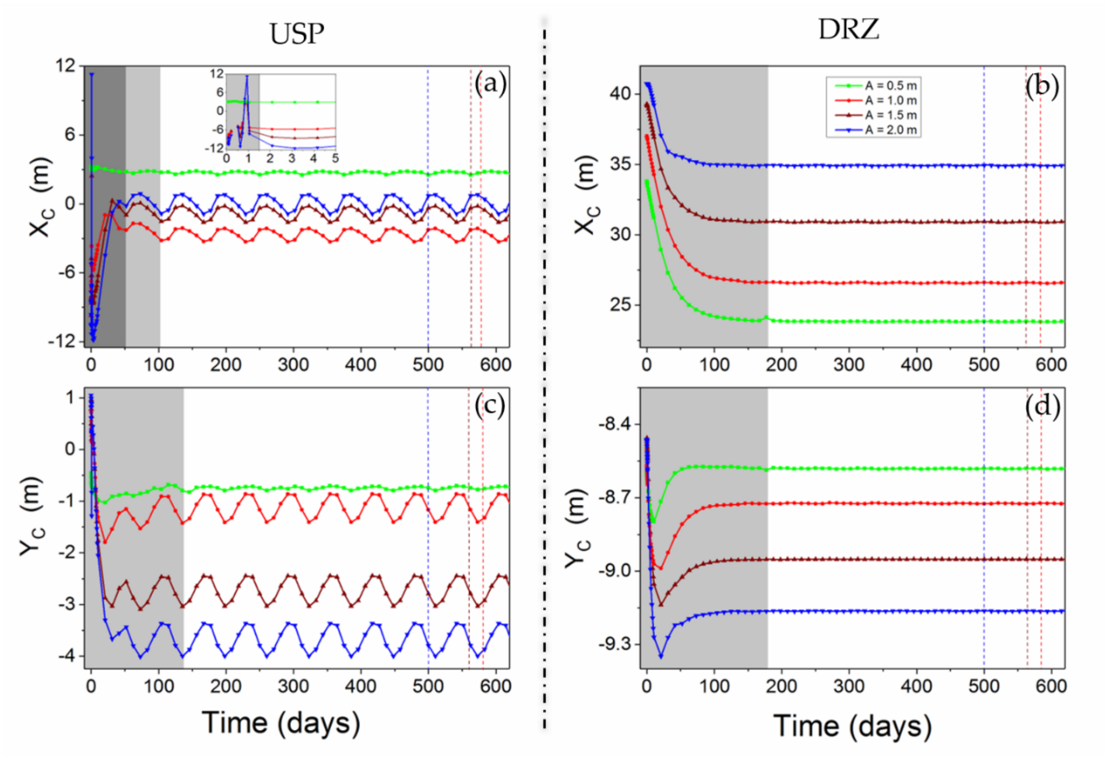

Fig. 4 Transient behavior of the horizontal (a, c) and vertical (b, d) components of the USP and DRZ mass center positon for various tidal fluctuations. Squares: A = 0.5 m; dots: A = 1.0 m; triangles: A = 1.5 m; inverted triangle: A = 2.0 m. The dashed line indicates the time for 1% difference between two adjacent time steps.

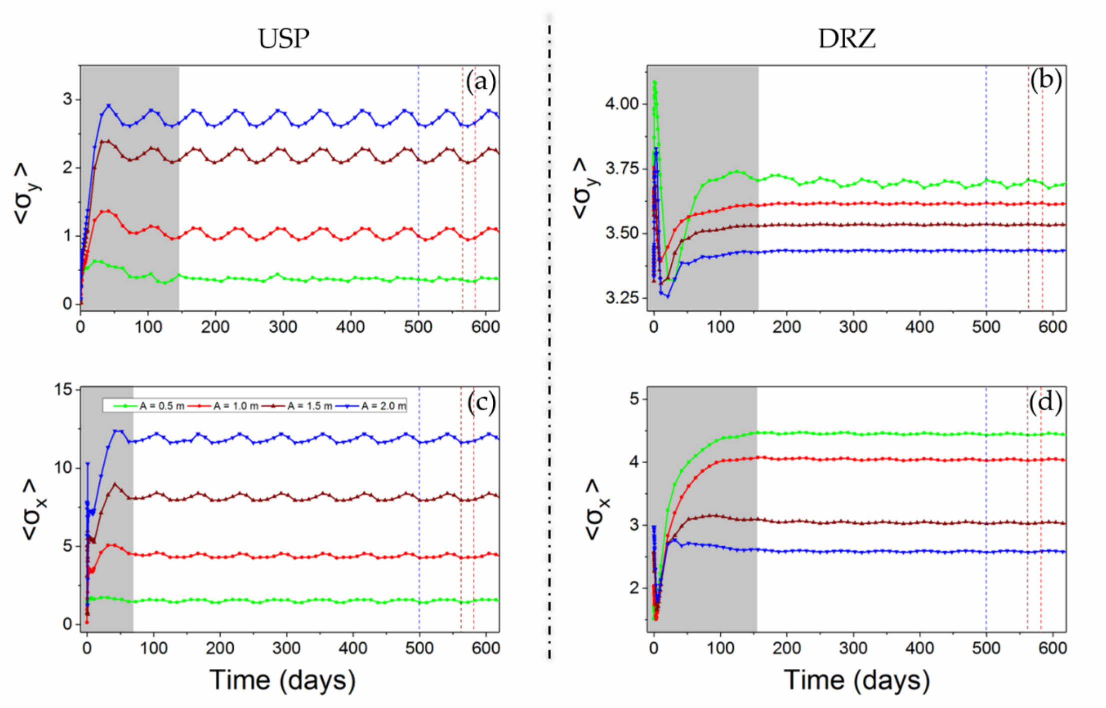

Figure 5. Transient behavior of the transverse mixing width (a, b) and the longitudinal mixing length (c, d) of the USP (a, c) and DRZ (b, d), for various tidal fluctuations. Squares: *A* = 0.5 m; dots: *A* = 1.0 m; triangles: *A* = 1.5 m; inverted triangle: *A* = 2.0 m. The dashed line indicates the time for 1% difference between two adjacent time steps.

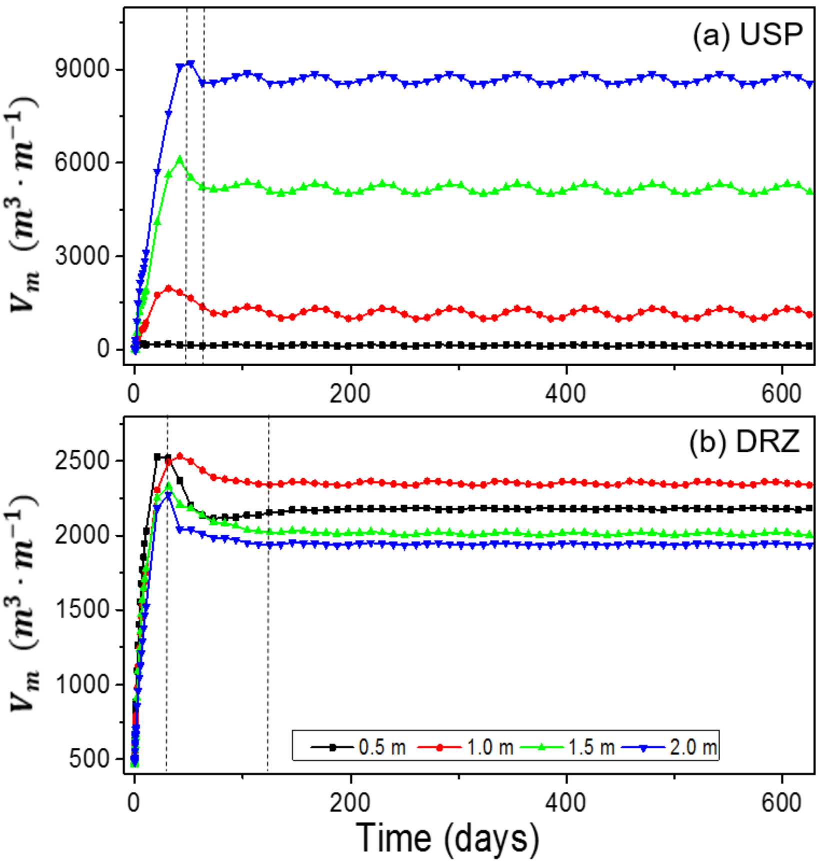

Fig. 6 Transient behavior of the mixing volume of the (a) USP and (b) DRZ for various tidal fluctuations. Squares: A = 0.5 m; dots: A = 1.0 m; triangles: A = 1.5 m; inverted triangle: A = 2.0 m.

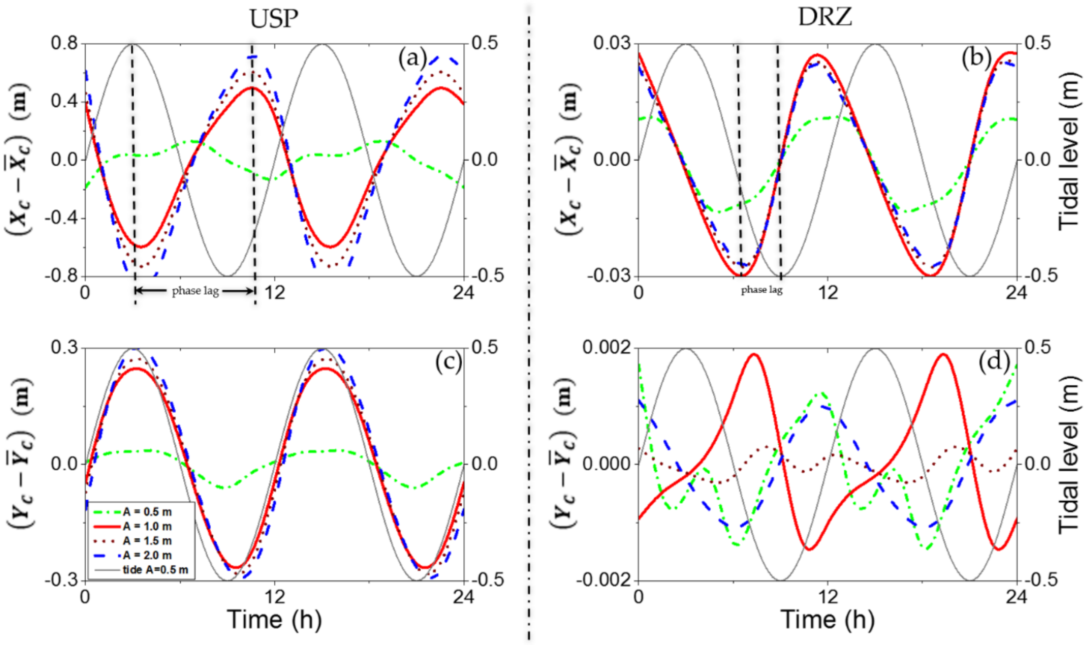

Figure 7. Daily cycle of the horizontal (a, b) and vertical (c, d) components of the USP (a, c) and DRZ (b, d) mass center position once the periodic quasi-steady state is reached, respectively, for different tidal amplitudes cases. The left vertical scale is for the mass center position, and the right vertical scale is for tidal level.

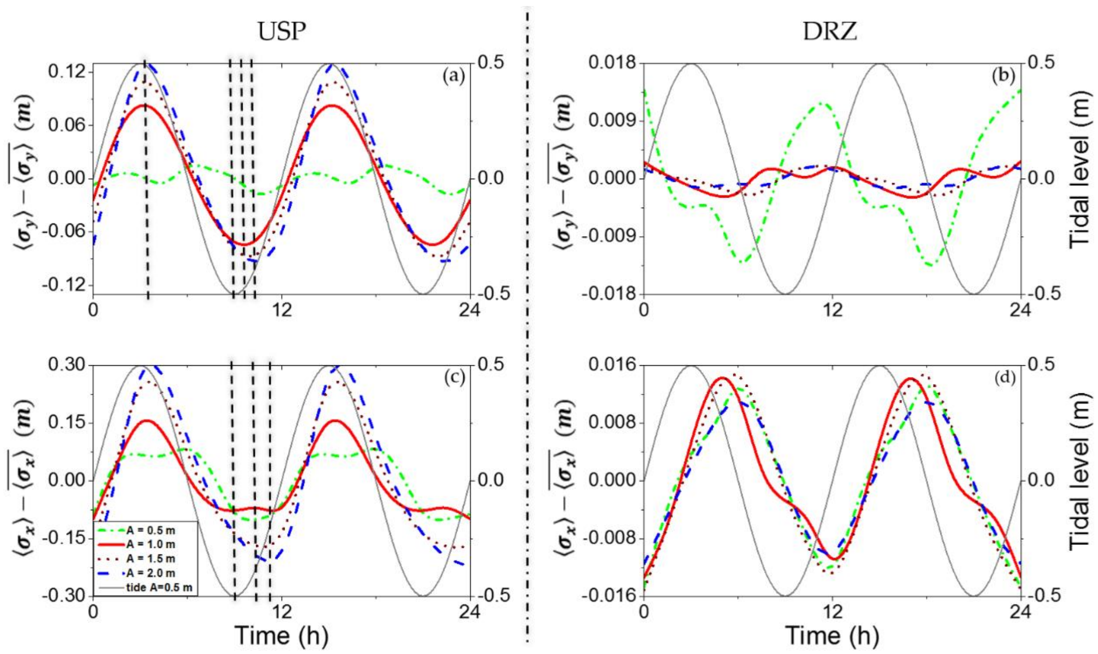

Figure 8. Daily cycle of the transverse mixing width (a, b) and the longitudinal mixing length (c, d) of the USP (a, c) and DRZ (b, d) around their mean value $\overline{\langle\sigma\rangle}$ once the periodic quasi-steady state is reached, respectively, for different tidal amplitude. The left vertical scale is for the mass center position, and the right vertical scale is for tidal level.

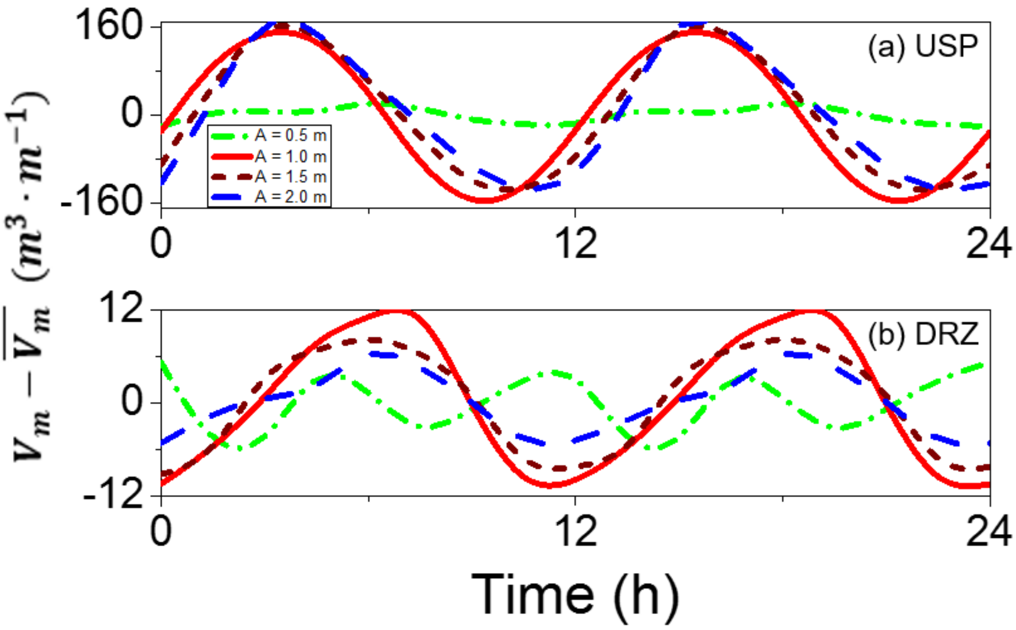

Figure 9. Daily cycle of the mixing volume of (a) USP and (b) DRZ once the periodic quasi-steady state is reached, respectively, for different tidal amplitude.

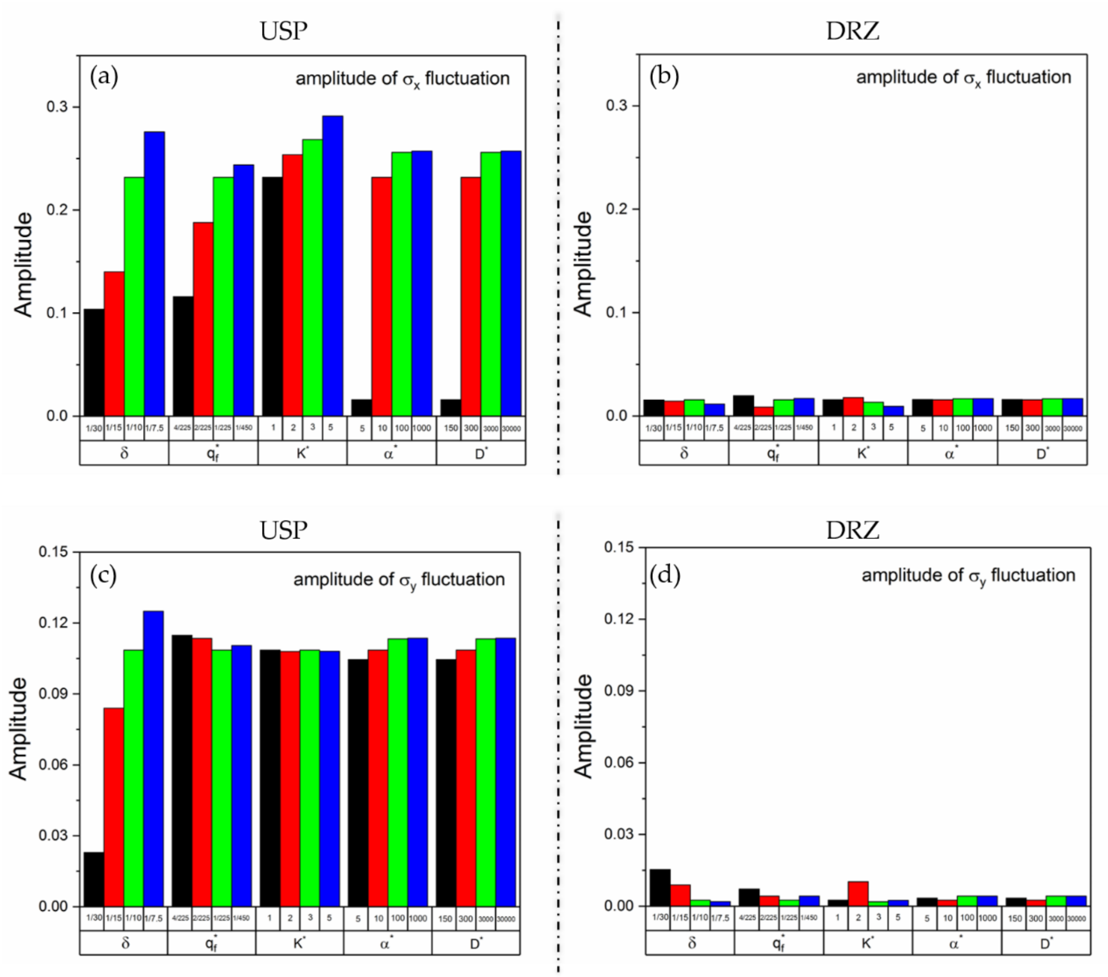

Figure 10. Compare of the fluctuation amplitude of longitudinal mixing length (a, b) and the fluctuation amplitude of transverse mixing width (c, d) of the USP (a, c) and DRZ (b, d) calculated based on the quasi-steady state results.